SAND2011-7894C
12PFL-0746

Investigation of Fuel Reactivity Stratification for Controlling PCI Heat-Release Rates Using High-Speed Chemiluminescence Imaging and Fuel Tracer Fluorescence

Author, co-author (Do NOT enter this information. It will be pulled from participant tab in MyTechZone)

Affiliation (Do NOT enter this information. It will be pulled from participant tab in MyTechZone)

ABSTRACT

Premixed charge compression ignition (PCI) strategies offer the potential for simultaneously low NOx and soot emissions with diesel-like efficiency. However, these strategies are generally confined to low loads due to inadequate control of combustion phasing and heat-release rate. One PCI strategy, dual-fuel reactivity-controlled compression ignition (RCCI), has been developed to control combustion phasing and rate of heat release. The RCCI concept uses in-cylinder blending of two fuels with different auto-ignition characteristics to achieve controlled high-efficiency clean combustion.

This study explores fuel reactivity stratification as a method to control the rate of heat release for PCI combustion. To introduce fuel reactivity stratification, the research engine is equipped with two fuel systems. A low-pressure (100 bar) gasoline direct injector (GDI) delivers iso-octane, and a higher pressure (600 bar) common-rail diesel direct-injector delivers n-heptane. A sweep of the common-rail injection timing creates a range of fuel reactivity stratification. A high-speed digital camera provides images of ignition and combustion luminosity, composed primarily of chemiluminescence. A quantitative laser-induced fuel-tracer fluorescence diagnostic also provides two-dimensional measurements of the mixture distribution prior to ignition. The injection timing sweep showed that the peak heat-release rate is highest for either early or late common-rail injection of n-heptane, and displays a minimum at mid-range injection timings near 50° BTDC. At very early injection timings, the optical data show that the charge is well mixed and overall fuel lean, so that it ignites volumetrically, resulting in rapid energy release. Conversely, when the injection timing is late in the cycle (near TDC), the mixing time is relatively short and much of the fuel-air mixture in the n-heptane jet is fuel-rich. Such mixtures that are near stoichiometric or richer have similar ignition delays, so that the charge ignites nearly instantaneously throughout the n-heptane jets. For the mid-range injection timings, at the minimum in the peak energy release rate, ignition occurs in the downstream portion of the n-heptane jet in localized auto-ignition pockets generated by the common-rail injection of n-heptane. The subsequent combustion process then progresses upstream toward the centrally mounted common-rail injector at a slower rate than either the early or late injection timings. In agreement with the observed combustion zone progression from the bowl-wall toward the injector, the fuel concentration measurements show that the fuel reactivity generally decreases from the bowl-wall toward the common-rail injector.

INTRODUCTION

Highly premixed compression-ignition strategies (e.g., homogenous-charge compression-ignition (HCCI)) offer attractive emissions and performance characteristics (i.e., high efficiency and low NOx and soot emissions) [1-7]. However, these operating strategies are generally confined to low engine loads due to inadequate control of both the heat-release rate and combustion phasing.

To address the issues with HCCI combustion phasing control, Bessonette et al. [8] performed experiments using fuels with a range of auto-ignition characteristics. Their findings suggest that the best fuel for HCCI operation may have an autoignition quality between that of diesel fuel and gasoline. Using a compression ratio of 12:1 and a fuel with a derived cetane number of ~27 (i.e., a gasoline boiling range fuel with an octane number of 80.7), they were able to extend the HCCI operating range to 16 bar BMEP – a 60% increase in the maximum achievable load compared to operation using traditional diesel fuel. Furthermore, their results showed that

low-load operation, below 2 bar BMEP, required a derived cetane number of ~45 (i.e., traditional diesel fuel). Thus, their results suggest that the fuel blending might allow HCCI to be optimized for specific operating conditions. Inagaki et al. [9] investigated dual-fuel PCI operation as a means for reducing the EGR requirements of PCI strategies. Using premixed iso-octane and direct injected diesel fuel, they were able to operate in PCI mode at 12 bar IMEP. Based on the work of Bessonette et al. [8] and Inagaki et al. [9], it is likely that different fuel blends will be optimal at different operating conditions (e.g., a high cetane fuel at light load and a low cetane fuel at high load). Thus, it may be desirable to have the capability to operate with fuel blends covering the spectrum from neat gasoline to neat diesel fuel depending on the operating regime.

Our previous work [3, 10] further explored the dual-fuel PCI approach of Inagaki et al. [9] (i.e., blending two fuels with different auto-ignition characteristics in-cylinder). Using metal engine experiments and CFD modeling, our previous work [2,3,10-15] showed that stratifying the fuel reactivity via in-cylinder fuel blending improves control over the heat-release rate (combustion phasing is controlled by the overall fuel reactivity and the combustion duration is controlled by spatial gradients in the fuel reactivity) and allows an extension of the PCI combustion regime to higher engine loads (up to 16.5 bar IMEP [2]) . Consequently, we termed this alternative combustion mode "reactivity-controlled compression-ignition," or RCCI. Further, the metal engine experiments have shown that RCCI combustion can achieve gross indicated efficiencies over 50 percent for a wide range of operating conditions while meeting current, heavy-duty, on-highway NOx and soot emissions limits in-cylinder. The high-efficiency is primarily due to reductions in heat transfer losses by avoiding high temperature regions [`15]. Although they are useful to understand emissions and performance tradeoffs, details of the dominant in-cylinder processes controlling RCCI combustion cannot be observed in metal engine experiments.

In an attempt to improve the fundamental understanding of RCCI combustion, Splitter et al. [14] used in-cylinder Fourier-transform infrared (FTIR) spectroscopy to investigate the evolution of the RCCI combustion process. FTIR spectra were acquired at two locations, to provide a degree of spatial resolution, and were indexed to engine crank-angle to give cycle-averaged, crank-angle-resolved in-cylinder spectroscopy. Their results suggest that the RCCI combustion process proceeds at different rates in different locations of the cylinder. However, their measurements were restricted by the limited optical access of their engine. Additionally, several studies have used detailed CFD modeling (e.g., Kokjohn et al. [15]) with reduced kinetics mechanisms to investigate RCCI combustion. The CFD modeling predicts that in-cylinder fuel blending creates non-uniformities in the auto-ignition characteristics of the charge (i.e., fuel reactivity) and thereby controls the heat-release rate. To further the understanding of the mechanisms controlling RCCI heat release, we used optical engine experiments to investigate ignition and reaction zone progression in an engine operating in the dual-fuel RCCI combustion mode [16]. High-speed chemiluminescence imaging showed that ignition generally occurs in the downstream portion of the jet – ignition sites were found both near the piston bowl rim and in the squish region. These ignition sites grew for several crank angle degrees and merged into larger reaction zones. In the same study, the fuel distribution prior to ignition was imaged with a fuel tracer fluorescence diagnostic. In agreement with the chemiluminescence study, the fuel distribution showed that the region of highest fuel reactivity was located above the piston bowl-rim. This study expands our previous work [16] and explores fuel reactivity stratification as a method to control the rate of heat release for PCI combustion using a heavy-duty, single cylinder, optically accessible research engine using a combination of high-speed chemiluminescence imaging and fuel-tracer planar laser-induced fluorescence (PLIF).

EXPERIMENTAL SETUP

ENGINE SPECIFICATIONS

A single-cylinder, direct-injection (DI), 4-stroke diesel engine based on a Cummins N14 production engine was used for this investigation. A schematic of the engine and optical setups are shown in Figure 1 and specifications are given in Table 1. A complete description of the engine is available in Refs. [17,18]. The research engine is typical of a heavy-duty diesel engine with a 13.97 cm bore and 15.24 cm stroke giving a displacement of 2.34 L per cylinder. The intake port geometry of the production engine, which has a steady-state (i.e., measured on a flow-bench) swirl ratio of 0.5 [19], is preserved in the research engine.

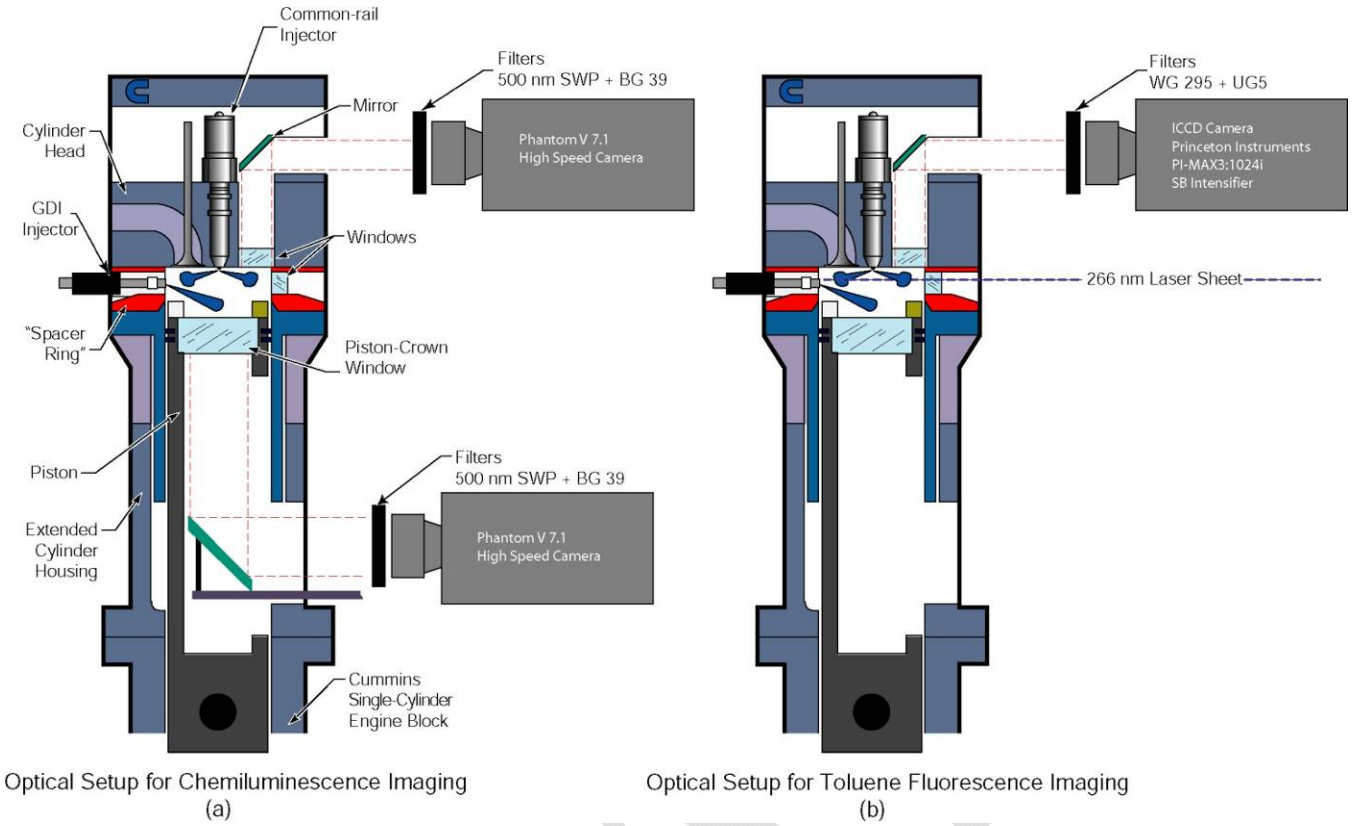

Figure 1. Schematic of the optically accessible research engine. (a) shows the camera setup for the high-speed chemiluminescence imaging study and (b) shows the camera and laser sheet setup for the fuel tracer PLIF study.

Table 1. Engine Specifications

Engine base type	Cummins N-14, DI diesel
Number of cylinders	1
Cycle	4-stroke
Number of intake valves	2
Number of exhaust valves	1[1]
Combustion chamber	Quiescent, direct injection
Swirl Ratio	0.5 (approximate)
Bore	13.97 cm [5.5 in]
Stroke	15.24 cm [6.0 in]
Bowl width	9.78 cm [3.58 in]
Displacement	2.34 liters [142 in^3]
Connecting rod length	30.48 cm [12.0 in]
Piston pin offset	None
Geometric compression ratio	10.75:1

[1] In this optically accessible diesel engine, one of the two exhaust valves of the production cylinder head has been replaced by a window and periscope

To allow optical access, the engine is equipped with an extended piston and the stock metal piston bowl has been replaced with a flat fused silica piston crown window. Further, one of the two exhaust valves has been replaced with a window, and a periscope mirror in the rocker box gives a view of the squish region (i.e., the region above the piston bowl-rim). Four windows are also located around the upper portion of the cylinder wall to allow cross-optical access for laser based diagnostics. Finally, to allow the laser sheet to penetrate into the combustion chamber when the piston was near TDC, a 37 mm wide section of the piston-bowl rim was removed as indicated in Figure 2.

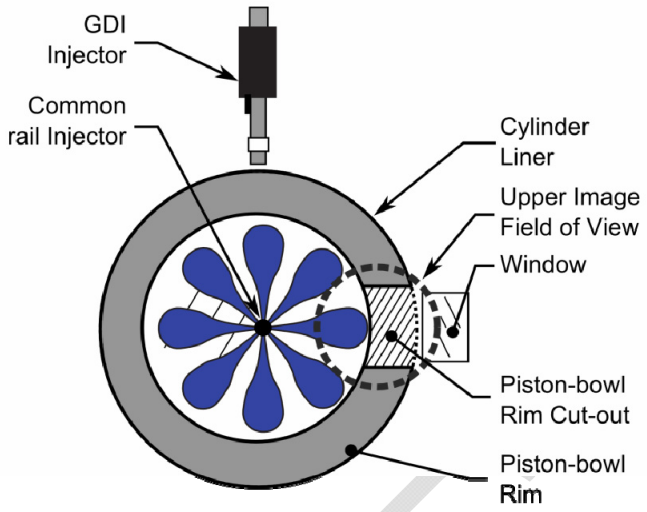

Figure 2. Top view of piston showing piston-bowl rim cut-out (hatched region) and the location of the cylinder head window field-of-view.

INJECTION SYSTEMS

RCCI combustion is achieved by using in-cylinder blending of two fuels with different auto-ignition characteristics, such as gasoline and diesel fuels. Multi-component gasoline and diesel fuels contain molecules that fluorescence when illuminated by ultraviolet light, which would interfere with the toluene fuel-tracer fluorescence diagnostic (described later). Hence, to facilitate the fuel-tracer measurements, purified gasoline primary reference fuel (PRF) components (i.e., n-heptane and iso-octane) were used because they display insignificant fluorescence interference. A charge of high-purity (99% or better) iso-octane was created using a gasoline direct injection (GDI) system. The GDI injector is mounted in a metal blank in place of one of the optical access windows formerly located in the cylinder liner (see Figure 1). The specifications of the GDI injector are provided in Table 1. The GDI has a 7-hole, asymmetric tip, with all seven holes located on one hemisphere of the injector. This hole layout prevented fuel impingement on the cylinder head when mounted in the cylinder wall window (i.e., perpendicular to the axis of the piston). HPLC-grade n-heptane was delivered through a Cummins XPI high-pressure, electronically-controlled, common-rail (CR) fuel injector with specifications given in Table 3. The injector is capable of multiple injections at up to 2000 bar injection pressure. For the present study, an 8-hole mini-sac tip was installed. Each hole of this tip, has a nominal orifice diameter of 140 microns with no hydrogrounding (i.e., the edges are sharp). The nozzle has an included angle of 152° (14° downward from the fire deck, i.e., the bottom surface of the cylinder head exposed to the combustion chamber). Finally, to minimize thermal loading, the engine was only fired 1 out of 10 cycles.

Table 2. Gasoline direct injector (GDI) specifications.

Injector type	Bosch GDI
Fuel	high-purity (99%+) iso-octane
Number of holes	7, asymmetric
Supply pressure	100 bar
Nominal orifice diameter	150 micron

Table 3. XPI common-rail (CR) fuel injector specs.

Injector type	common-rail, solenoid actuated
Fuel	HPLC-grade n-heptane
Cup (tip) type	mini-sac
Number of holes	8, equally spaced
Included angle	152°
Rail pressure	600 bar
Orifice treatment	none (square-edged)
Nominal orifice diameter	140 micron

OPERATING CONDITION

The engine operating conditions for the chemiluminescence imaging study are shown in Table 4. The engine was operated at a speed of 1200 rev/min and a gross indicated mean effective pressure (IMEP) of 4.2 bar. This light-load condition was chosen to allow exploration of a wide range of conditions without damaging the large piston crown window.

With the intent of creating a well-mixed charge, 41 mg of iso-octane was delivered through the GDI injector at -240° ATDC (during the intake stroke) at an injection pressure of 100 bar. The n-heptane was delivered through the common-rail injector at a pressure of 600 bar. A sweep of common-rail start of injection timings was used to generate a range of fuel distributions from well mixed (i.e., early common-rail injection) to stratified (i.e., late common-rail injection)[1]. The total injected mass of n-heptane was 23 mg/cycle for all experiments in this work. The engine was operated without dilution (i.e., the inlet oxygen concentration was 21% by volume) and the intake temperature was adjusted at each injection timing to hold combustion phasing (CA50) fixed at 2° ATDC in order to allow direct comparisons of the combustion rate. The air flowrate was held constant at 23 g/s for each case, resulting in an intake pressure near 1.1 bar absolute and a relatively low TDC density of 11.1 kg/m^3 for the low-load conditions of this study.

The toluene fuel-tracer fluorescence study was conducted at the same thermodynamic conditions as the chemiluminescence imaging study; however, to avoid complications from oxygen quenching of the toluene fluorescence, the intake was supplied with 100% nitrogen. Further, HPLC n-heptane doped with 1% toluene was used in both the GDI and common-rail fuel systems for quantitative fuel distribution measurements. The same toluene-doped n-heptane was used in both fuel systems (non-combusting conditions) to avoid uncertainties in the toluene fluorescence yield in different solvents.

Table 4. Engine operating condition for the chemiluminescence imaging study and reference operating condition for the toluene fuel tracer fluorescence study.

Engine speed	1200 rpm
Gross IMEP	4.2 bar
Intake temperature	73°C to 100°C
Intake pressure	1.1 bar abs.
Intake flowrate	23.0 g/s
Inlet oxygen concentration	21 vol. %
GDI injection pressure	100 bar
CR injection pressure	600 bar
GDI SOI (command)	-240° ATDC
CR SOI (actual)	-155° to -15° ATDC
Actual GDI DOI	36° CA
Actual CR DOI	9° CA
Total injected fuel mass	64 mg
iso-octane mass (GDI)	64%
n-heptane mass (CR)	36%
Premixed (iso-octane) equivalence ratio	0.27
Overall equivalence ratio	0.42
Nom. motored TDC density	11.1 kg/m^3

[1] The purpose of this work is not to optimize the injection timing, but rather show the influence of fuel reactivity stratification on the heat-release rate. Liquid impingement on the cylinder liner was observed for injection timings earlier than -90° ATDC; however, since n-heptane was used as the common-rail fuel and the intake and coolant temperatures were set near the atmospheric boiling point of n-heptane, it is expected that any liquid impinging on the liner will quickly vaporize. The high-speed imaging showed very little evidence of the "pool fires" characteristic of liquid films. Of course, if diesel fuel were used as the common-rail fuel, it is expected that liquid impingement would be problematic; however, it is likely that, even using diesel fuel, a multiple injection strategy could be used to generate a range of fuel reactivity stratification. Such an investigation, however, is beyond the scope of this study.

CONVENTIONAL DATA ACQUISITION

Cylinder pressure was measured with an AVL QC43D piezoelectric transducer at ¼° crank angle increments and the measurements were set to match (pegged to) the intake pressure near bottom dead center (BDC). The apparent heat-release rate (AHRR) was calculated from the measured pressure data using the standard first-law analysis (e.g., Heywood [20]) with constant gas properties. Prior to calculating the AHRR, the cylinder pressure data were smoothed using a Fourier series low-pass filter with a Gaussian roll-off function having a transmission of 100% from 0 to 800 Hz and dropping to 1% at 3360 Hz.

COMBUSTION LUMINOSITY IMAGING

Crank-angle resolved combustion luminosity was recorded with an unintensified Phantom 7.1 complementary metal oxide semiconductor (CMOS) high-speed camera (HSC) using a 50-mm glass Nikkor lens with the aperture fully open (f/1.2). Because a glass lens was used, chemiluminescence in the ultra-violet (UV) range is not recorded (i.e., OH* does not contribute to the images presented). Furthermore, a combination of a 500 nm short-wave pass (SWP) filter and a BG39 colored glass filter were used to reject long-wavelength (green through IR) soot luminosity (if present). The recorded luminosity is likely chemiluminescence from CH_2O*, HCO*, CH*, and CO_2* and broadband emission from the CO continuum [21, 22]. The HSC images were acquired with a resolution of 512 x 512 pixels with a spatial resolution of 3.9 pixel per mm, and the exposure time for each frame was 125 µs. The long exposure time was required to collect reasonable light levels with the non-intensified HSC used in this study. Although the long exposure time results in a small amount of smearing for cases showing rapid energy release, the smearing does not influence the conclusions of the study.

FUEL-TRACER FLUORESCENCE IMAGING

Quantitative fuel-vapor concentrations were measured using toluene fuel-tracer fluorescence. As previously discussed, the n-heptane used for the fuel-tracer fluorescence imaging study was doped with toluene at a concentration of 1% by volume. Previous work (e.g., Genzale et al. **[19]**) showed that this toluene concentration provided a good balance between signal strength and attenuation of the laser light. The toluene fluorescence was excited by the 266-nm output of a frequency-quadrupled Nd:YAG laser. The laser beam was formed into a thin sheet (less than 1 mm thick) using a combination of a negative cylindrical lens (f = -50 mm) and positive plano-spherical lens (f = 500 mm). The low-intensity tails on either end of the sheet were clipped to leave the center of the beam, with relatively uniform intensity. After being clipped, the sheet passing through the window was approximately 31 mm wide with a remaining energy of 26 mJ per pulse. All of the images presented in this study were acquired with the sheet positioned 13 mm below the firedeck (i.e., the flat bottom surface of the cylinder-head).

A blue-optimized, intensified CCD camera (Princeton Instruments PI-MAX3:1024i SB) with a 55 mm f/3.5 UV lens with the aperture fully open imaged the resulting florescence viewing downward through the cylinder head window (see Figure 1). The intensifier gate was set to the minimum practically achievable (approximately 200 ns). A WG295 long-wave pass (LWP) filter helped to isolate the toluene fluorescence (265-330 nm) from scattered laser light. Additionally, a UG5 UV-bandpass filter (passband in the range of 220 to 400 nm) blocked red-shifted fluorescence from motor oil and other sources [22].

Quantitative fuel-vapor concentration measurements require calibration of the fluorescence signals with a known fuel/tracer concentration. In this work, calibration images at a known fuel/tracer concentration were obtained by injecting toluene-doped n-heptane, using the common-rail injector, near TDC of the intake stroke. In similar studies (e.g., Musculus et al. [23]) early-cycle injections of low boiling-range fuels have been shown to yield acceptably homogenous mixtures during the compression stroke. Indeed, the calibration images from this study (e.g., Fig. 3) appear reasonably uniform. Although the calibration images appear nearly homogeneous, it is possible that non-uniformities exist outside of the camera field of view. These non-uniformities, if present, introduce uncertainty into the vapor fuel concentration measurements of this study, though it is not possible to quantify this level of uncertainty in the present work. Further, with the early-cycle injection used in this study, some liquid may impinge on the combustion chamber surfaces; however, the intake temperature and coolant temperature were set to near the atmospheric boiling point of n-heptane. Thus, it is likely that any liquid impinging on a combustion chamber surface would rapidly vaporize. However, should liquid fuel remain at the imaging time, the fuel vapor concentration measurements would be biased towards higher fuel concentrations.

Fuel-vapor concentrations were measured for separate injections from both the common-rail and GDI fuel systems. At each crank angle of interest, images were acquired in sets of four. The first image had no fuel injection and recorded background fluorescence interference – likely due to residual lubrication oil excited by scattered laser light [22, 23]. The second image provided a flat-field calibration at a known toluene/fuel concentration as previously discussed. The third and fourth images recorded fluorescence from the

fuel injected through the GDI only and common-rail injector only, respectively. This four-image sequence was repeated 40 times at each crank angle of interest. Figure 3 shows a representative image sequence.

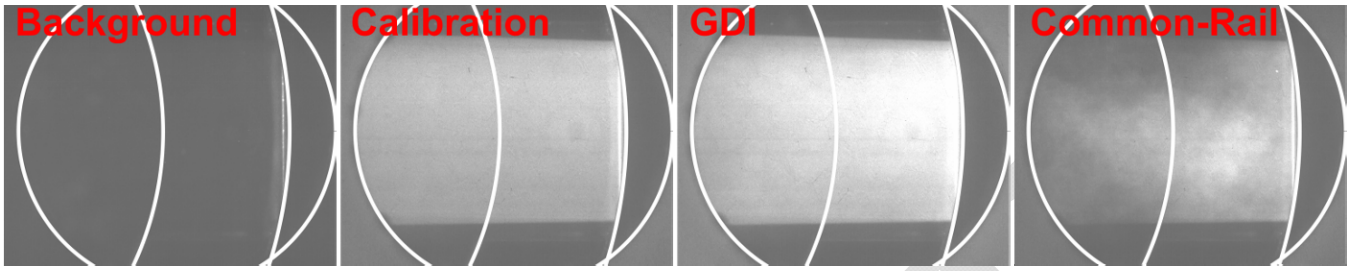

Figure 3. Typical image acquisition sequence for the toluene fuel-tracer PLIF diagnostic. The images were acquired at -5° ATDC for a case with a CR SOI timing of -50° ATDC.

To extract quantitative information using LIF, the photophysics of the LIF signal must be understood. The engine was operated using 100% N_2 for the fluorescence measurements to avoid the collisional quenching by oxygen, but two primary concerns remain: temperature dependence of the fluorescence quantum yield and absorption cross section, and potential pressure dependence due to collisional quenching with N_2 and fuel [24].

In a review paper, Schulz et al. [24] showed that, under 266 nm excitation, the absorption cross section increases by more than a factor of three when the temperature is increased from 300 to 1000 K. Further, the fluorescence quantum yield over the same temperature range decreases by two orders of magnitude. At the image acquisition time, the temperatures of the calibration and raw data images are slightly different due to differences in the fuel concentrations (i.e., differences in the evaporative cooling and in the compression heating). Therefore, it is important to correct the images for temperature prior to conversion to a fuel concentration. The temperature dependence of toluene fluorescence was evaluated under well-mixed conditions (i.e., common-rail fuel injection at -345° ATDC) over a range of temperatures. Figure 4 shows the relative toluene fluorescence evaluated over a range of in-cylinder temperatures from 550 K to 940 K. Following the work of Musculus et al. [23], an offset exponential was fit to the data and used as a calibration curve.

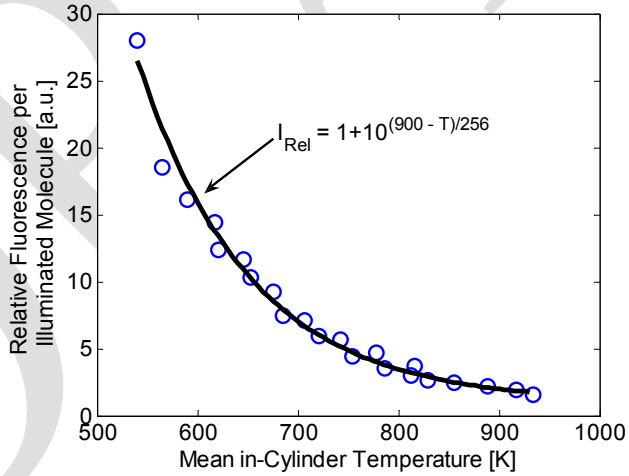

Figure 4. Relative toluene fluorescence as a function of mean in-cylinder temperature. The fueling was held constant at 39 mg/inj.

Similar to the temperature dependence, the pressure dependence was evaluated over a range of conditions. Consistent with the findings of Musculus et al. [23], the toluene LIF signal was shown to be independent of pressure after temperature corrections were applied.

With the pressure and temperature dependence known, the images were processed with the iterative procedure outlined in Figure 5. Initially, the fuel distribution was calculated by assuming a uniform temperature distribution at the image acquisition time. The temperature fields of the calibration and data images (i.e., GDI or CR images) are different due to evaporative cooling and changes in

the specific heats of the mixture due to the differences in fuel concentrations. To account for the temperature dependence of toluene fluorescence, the fluorescence intensity of each data image was corrected for the local temperature difference from the calibration image by

$$I_{corrected\_pixel} = I_{data\_raw\_pixel} \frac{I_{rel}\left(T_{cal}\right)}{I_{rel}\left(T_{data\_pixel}\right)}, \quad \textbf{(1)}$$

where $I_{corrected\_pixel}$ is the corrected fluorescence intensity of the data image, $I_{data\_raw\_pixel}$ is the local fluorescence intensity of the GDI or common-rail image, $I_{rel}(T_{cal})$ was calculated from the temperature calibration curve given in Fig. 4 at the average temperature of the calibration image, and $I_{rel}(T_{data\_pixel})$ was calculated from the temperature calibration curve at the local temperature of the data image. Then, the fuel distribution was calculated by normalizing the corrected fluorescence intensity by the flat field calibration image as shown in Eq. 2

$$n_{data} = n_{calibration} \frac{I_{corrected\_pixel}}{I_{calibration\_pixel}} \quad \textbf{(2)}$$

In Eq. 2, n_{data} is the local fuel vapor molar density and $n_{calibration}$ is fuel vapor molar density of the calibration image.

The above procedure provides an initial estimate of the fuel distribution. The final fuel distribution was calculated iteratively as follows. First, the temperature of the N_2 charge at BDC was adjusted from the intake stream temperature to account for heat transfer during induction according to the procedure of Sjöberg et al. [25]. Second, the rise in temperature of the charge of N_2 due to compression from BDC to the SOI timing was calculated by numerical integration assuming adiabatic compression according to the measured pressure rise. The compression calculation accounted for variable specific heats. In this way, the resulting temperature represents the adiabatic core of the charge. Third, the fuel was assumed to be injected and mixed at the SOI timing. The charge of N_2 and fuel was then compressed from the SOI timing to the image timing assuming that the fuel distribution remains frozen. Although the real fuel distribution is not actually frozen, this simplification in the calculation provides a method to account for the temperature distribution resulting from the different heat capacities of N_2 and n-heptane (Hwang et al. [22] showed the importance of considering the change in specific heats due to differences mixture composition). The image was then corrected again for temperature as discussed above. This procedure was looped until convergence was obtained in the fuel distribution.

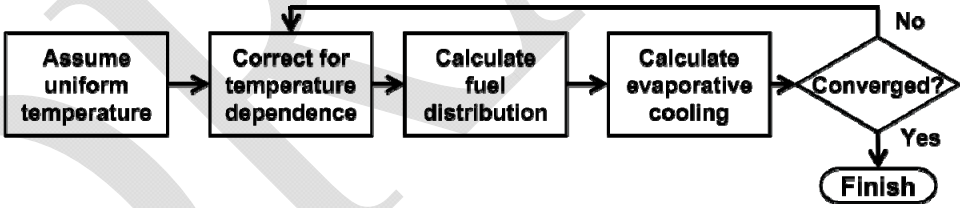

Figure 5. Image processing procedure for toluene fuel tracer fluorescence imaging.

The fuel distributions of the GDI and common-rail injections were then ensemble averaged over 40 images and average fuel-distribution maps were generated. Of particular interest to this study are the relative concentrations of fuel from the GDI and common-rail fuel streams. Thus, a PRF number is defined as

$$PRF = 100 \frac{m_{GDI} / \rho_{\text{iso-octane}}}{m_{GDI} / \rho_{\text{iso-octane}} + m_{CR} / \rho_{\text{n-heptane}}}, \quad \textbf{(3)}$$

where the m_{GDI} is the measured vapor-fuel mass from the GDI images corrected for the difference in molecular weight of iso-octane and n-heptane, m_{CR} is the mass of n-heptane measured from the common-rail (CR) injection images, and $\rho_{\text{iso-octane}}$ and $\rho_{\text{n-heptane}}$ are the densities of liquid iso-octane and n-heptane, respectively. This definition of PRF number is equivalent to a volume percent (by liquid) of iso-octane (i.e., the local octane number) in the fuel blend for each pixel.

RESULTS AND DISCUSSION

HEAT-RELEASE RATE

Figure 6 shows the effect of CR SOI timing on the peak apparent heat-release rate. Notice that the peak apparent heat-release rate tends to increase significantly at both early and late CR SOI timings and a minimum is observed near an intermediate CR SOI timing of -50° ATDC. Figure 7 shows the ensemble-averaged apparent heat-release rates for cases with CR SOI timings of -145°, -50°, and -15° ATDC. At an early common-rail SOI timing (-145° ATDC) the low-temperature heat release (LTHR) begins around 19° BTDC, reaches a peak near -15° ATDC, and ends at -11° ATDC. Second-stage ignition begins near -4° ATDC and the AHRR peaks around 2° ATDC. Following the peak, the AHRR falls off rapidly until about 7.5° ATDC, followed by a small tail until about 12° ATDC. The tail may be the result of several different effects. First, reactions in the boundary layer likely occur last due to the lower temperatures and may occur at a lower rate due to both lower temperatures and the influence of heat transfer. Next, although both the GDI and common-rail injection timings occur very early in the cycle, inhomogeneities in the fuel-air mixture certainly exist. Thus, the tail may be due to either locally rich or excessively lean regions where combustion struggles to reach completion. Given the very early common-rail injection timing, rich regions may exist where liquid fuel impinges on either the piston surface or cylinder liner. Lean regions are likely the result of inhomogeneities present in the premixed iso-octane (i.e., from the GDI injection). The engine used in this study has a relatively large ring-pack crevice region and both fuel injection events occur early in the cycle; therefore, it is also possible that the tail is due to ring-pack crevice outgassing. However, in this case the peak pressure occurs near 6.5° ATDC. Since the tail begins around 7.5° ATDC and ends by approximately 12° ATDC – only slightly after the observed peak in the cylinder pressure – it is not likely that ring-pack crevice outgassing is responsible.

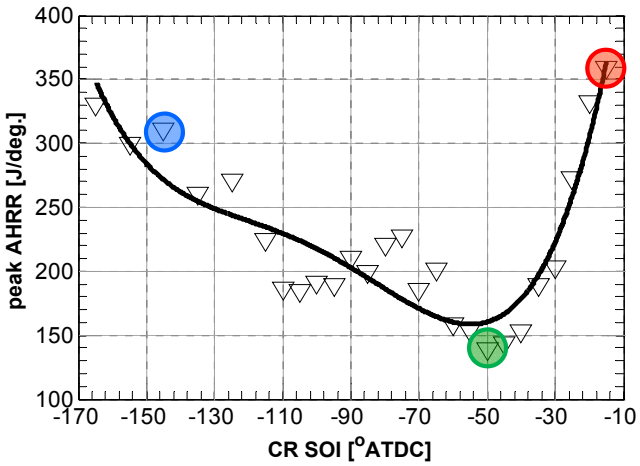

Figure 6. Effect of CR SOI timing on the peak AHRR. The colored circles show selected cases for further analysis.

Similar to the early-injection timing, the case with a CR SOI timing of -50° ATDC also shows that LTHR begins near -19° ATDC. The LTHR peaks at -14° ATDC and reaches completion by -10° ATDC. In contrast to the early-injection timing, the delay between the end of LTHR and start of HTHR is relatively short. HTHR begins at -7° ATDC and proceeds relatively slowly, peaking near TDC. Recall that as was shown in Figure 6, the peak AHRR is approximately half that of the earliest or latest injection timing cases. Similar to the slow rise in the AHRR, the end of combustion also occurs at a relatively slow rate.

The latest injection timing case (SOI -15° ATDC) shows that LTHR begins around -5° ATDC and peaks around -3.5° ATDC. The end of LTHR is much less clear for the latest injection timing case. Although the average AHRR trace shows a "dip" near -2° ATDC which could signify the end of LTHR, this feature was not observed for all cycles. Regardless, the latest injection case shows a very quick transition to second-stage ignition followed by a rapid spike in heat release. The peak AHRR occurs at 1.75° ATDC. Following the peak, the heat release falls off rapidly until 6° ATDC. In this case, a long tail on the AHRR curve is observed and heat release remains elevated to later than 20° ATDC.

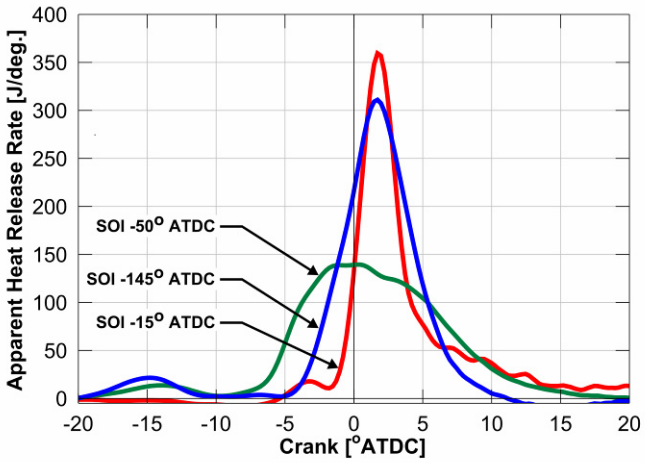

Figure 7. Apparent heat-release rates for the selected cases.

COMBUSTION LUMINOSITY IMAGES

To understand the observed differences in the AHRR curves for the different injection timings, high-speed camera sequences showing high-temperature chemiluminescence were recorded. The image sequences for the three selected injection timings are shown in Figure 8. The camera settings were held fixed for all operating conditions. The images are acquired with the high-speed camera viewing upward through the flat piston crown window. The centrally mounted common-rail fuel injector is visible in the center of the images and the solid white line on outer edge of the images indicates the location of the piston bowl rim. The dashed white line near the 3 o'clock position shows the overlapping field-of-view of the cylinder head window. The GDI injector is located at the 12 o'clock position and delivers a spray downwards from the perspective of the camera. The number in the upper left-hand corner of each image shows the crank angle at which the image was acquired. The first image in each sequence shows the CR fuel spray illuminated by a high-powered LED at 3 degrees after SOI (ASOI). Also, recall that the piston bowl has a cutout at the three o'clock position to allow laser access for the fuel-tracer fluorescence diagnostic. The image sequences presented here are from a representative single cycle. The representative cycle was selected as the cycle that has the minimum sum of the squared error with respect to the average AHRR curve and the comparison between the single-cycle and ensemble average heat-release rates are shown at the top of each image sequence.

Discussion of the combustion luminosity images begins with the case with an SOI of -145° ATDC. One image of the spray during CR injection is included at the beginning of the image sequence. The spray penetration for such early injection into low-density gases is quite long, extending nearly to the bowl-rim even with high-volatility n-heptane. Some variation in the penetration among the sprays seems apparent, but the sprays are not illuminated uniformly, so some of the variation in the liquid fuel penetration may be an optical artifact. Some of the variation may also be due to dynamics of the needle with only partial lifts for the relatively short injections for these conditions. Ignition is observed near -5° ATDC at several locations on the right half of the field of view. After ignition, the reaction zone grows rapidly, which is consistent with the observed rapid energy release. By -2° ATDC the reaction zone fills approximately half of the field of view. Notice that auto-ignition sites are now visible near the nine o'clock position and by 1° ATDC the luminosity is present nearly all the way across the field-of-view. For the selected case, ignition was first observed on the right-hand side of the chamber, suggesting that the reactivity of the right side of the chamber is slightly higher than that of the left; however, not all image sequences showed auto-ignition favoring the right side of the chamber. Moreover, the random ignition locations and rapid reaction zone growth suggests little stratification in fuel reactivity.

The second column of Figure 8 shows combustion luminosity images for the case with a common-rail SOI timing of -50° ATDC. Similar to the early injection timing, the liquid sprays penetration is uneven among the holes, due to non-uniform illumination and/or needle dynamics, but the overall penetration is much shorter at the higher in-cylinder density. Luminosity first appears near the piston bowl rim at -6° ATDC. Note that since the presented images are two-dimensional projections of three-dimensional reaction zones, the location of ignition with respect to the firedeck (i.e., into the page) cannot be determined. However, additional imaging into the squish region (not presented here for brevity), with the camera viewing downward through the cylinder head window as shown in Figure 1, showed that ignition generally occurred in the squish region near -6° ATDC. At -4° ATDC, luminosity is observed from five of the eight fuel jets, and similar to the image at -6° ATDC, luminosity is first observed near the edge of the piston bowl-rim. By 2° ATDC,

all eight fuel jets show at least weak luminosity. In contrast to the early injection case, once ignition occurs, the reaction zone does not rapidly progress throughout the chamber, but rather moves at a relatively steady rate from the bowl rim to the center of the chamber. This is observed in the images from TDC to 5° ATDC. Careful inspection of the image sequences reveals that the reaction zones are not continuous and that auto-ignition pockets appear ahead of the main or largest reaction zones. These auto-ignition pockets then grow and merge with the surrounding reaction zones. The observed broad combustion duration of the case with a common-rail SOI timing of -50° ATDC appears to be the result of staged or sequential auto-ignition from the downstream portion of the jet to the center of the combustion chamber.

Dec et al. **[26]** attributed similar sequential auto-ignition to an inhomogeneous temperature distribution. In the present study, the temperature distribution is undoubtedly affected by the common-rail injection event and therefore likely changes as the injection timing changes. However, since ignition occurs first in regions corresponding to the locations of the fuel jets, and since it is likely that fuel vaporization causes these regions to be cooler than the surrounding charge, the inhomogeneity of the temperature distribution is not a logical explanation for the observed broad combustion duration in the current study. In addition to temperature stratification, Sjöberg et al. **[27]** also showed that equivalence-ratio stratification can control the HCCI combustion duration. In the case of an inhomogeneous fuel distribution, they showed that combustion tended to progress from regions of higher equivalence ratio to regions of lower equivalence ratio. In the present study, the direct injection of n-heptane into a well-mixed charge of iso-octane generates gradients in both equivalence ratio and PRF number (i.e., reactivity). Contrary to the competing effects of the temperature and fuel distributions, the equivalence ratio and fuel-reactivity distributions are complimentary. That is, neglecting inhomogeneities in the background iso-octane distribution, the regions with the highest n-heptane concentrations have both the highest equivalence ratios and the highest fuel reactivity. As will be discussed in the mixing measurements section, spatial inhomogeneity in the fuel distribution (i.e., equivalence ratio and PRF number) is likely the dominant mechanism controlling the rate of energy release. The relative roles of equivalence ratio and PRF stratification are discussed in Appendix A.

The third column of Figure 8 shows combustion luminosity images for the case with a common-rail SOI timing of -15° ATDC. Again, the liquid sprays penetration appears uneven among the holes for the reasons already discussed, and the overall penetration for the high-volatility n-heptane sprays are very short at the high charge-density, near-TDC conditions. The injection ends near -6° ATDC (not shown) and luminosity is first observed at -1° ATDC near the piston bowl-rim. Once ignition occurs in the downstream region of a jet, the combustion zone rapidly progresses to fill the jet. The rapid progression of combustion throughout the jet suggests that much of the jet has a similar ignitability. This is in contrast to the previous case (i.e., the case with a common-rail SOI at -50° ATDC) where it was shown that the reaction zone moved slowly from the bowl rim to the center of the chamber. By TDC, seven of the eight jets display strong luminosity. Note that at TDC, luminosity for the one o'clock jet is much weaker than for the other jets. Such asymmetric ignition from jet to jet is typical, with different jets igniting late on different cycles. At 1° ATDC, high-intensity luminosity fills all eight jets. The late-SOI case has much higher intensity than the two other selected cases, which saturates the camera in the downstream portion of each jet. Due to the relatively late SOI timing, the strong luminosity is most likely due to natural soot incandescence from fuel-rich regions. Although exhaust emissions were not measured, the high-intensity luminosity suggests rich mixtures exist, which also implies stoichiometric mixtures with significant thermal NOx formation. Hence, the late injection timing case should have higher NOx emissions, and likely higher soot emissions than the earlier injection timing cases. Indeed, metal engine experiments [28] at a similar condition showed a significant increase in engine-out NOx and soot emissions as the injection timing was retarded to -15° ATDC. Further, notice that the highest intensity regions are confined to the fuel jets and weaker luminosity is observed between the jets. The weaker luminosity is likely due to chemiluminescence in the premixed iso-octane. At 4° ATDC the total luminosity begins to decrease and the brightest regions are confined to the downstream portion of the jet (i.e., near the piston bowl rim), and strong luminosity is observed near the piston bowl rim late into the expansion stroke (not shown).

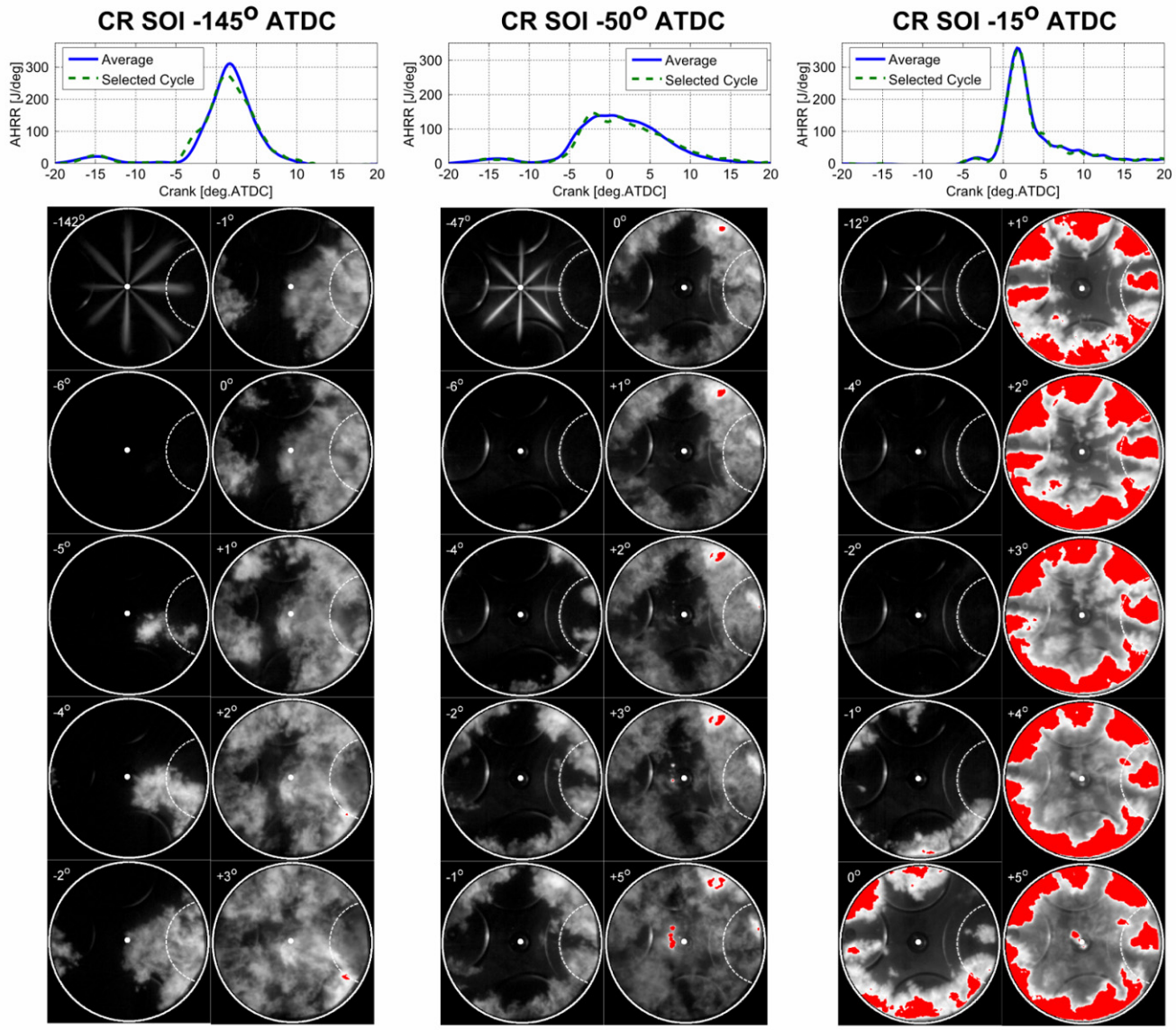

Figure 8. High speed movie sequence showing liquid fuel sprays and natural luminosity for the cases with common-rail SOI timings of -155°,-50°, and -15° ATDC. The number in the upper left-hand corner of each image shows the crank angle at which the image was acquired. The camera settings are the same for each operating condition. Regions colored red indicate saturation.

MIXING MEASUREMENTS

The high-speed combustion luminosity imaging in Fig. 8 shows distinctly different combustion events for the early-, mid- , and late-SOI timings. The differences in combustion characteristics are likely due to differences in the mixing times of the three cases. That is, the early-SOI timing results in rapid energy release due to an less stratified charge and the late-SOI timing results in rapid energy release due to an more stratified charge. From a practical perspective, these two limiting cases suggest controlling charge stratification using two fuels with different auto-ignition characteristics can be used to control PCI combustion heat release. To understand the influence of fuel reactivity stratification, the fuel tracer fluorescence diagnostic was used to evaluate the mixture stratification (both PRF and equivalence ratio) for the three cases previously discussed. In general, ignition occurred in the downstream portion of the jet near the bowl wall. The close proximity to the bowl wall suggests that ignition may occur in the squish region not visible through the piston bowl window. Therefore, we chose to collect the fuel tracer fluorescence images with the camera viewing downward through the cylinder head window and into the squish region, as described in Figure 1. Figure 9 shows the image layout. The left hand side of the PLIF image is bounded by the inner edge of the field-of-view at approximately 30 mm from the injector axis. Moving from left-to-right, the first solid grey line (smaller diameter) shows the inner edge of the piston-bowl rim and

the second solid grey line (larger diameter) shows the edge of the cylinder liner. In each image, the laser sheet enters on the right and exits on the left.

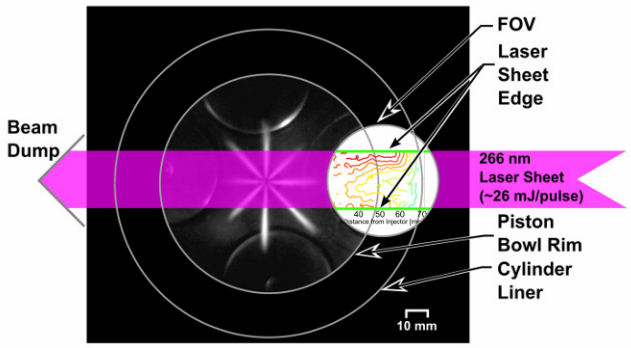

Figure 9. Field-of-view (FOV) for toluene fuel-tracer PLIF imaging. The image shows an overlay of the liquid fuel illuminated by a high-power LED and the resulting PRF map generated from the toluene fuel-tracer PLIF imaging. In the presented images, the laser sheet enters on the right and exits on the left.

The fuel distributions are compared at -5° ATDC (i.e., near the onset of high-temperature heat release). Images recorded at -21° ATDC (i.e., slightly before LTHR for the cases with SOI timings of -145° and -50° ATDC) are included in Fig. B2 of Appendix B. The ensemble-averaged fuel distributions are discussed first and are then compared to single-shot images to highlight local phenomena controlling the combustion characteristics.

Figure 10 shows the ensemble-averaged PRF and equivalence ratio distributions at -5° ATDC for the three selected cases. To improve the interpretation of the PRF and equivalence ratio distributions, Figure 11 shows the corresponding average PRF and equivalence ratio as a function of axial distance from the injector. The solid lines show the average in the radial direction (y-direction in the PRF and equivalence ratio maps of Figure 11) and the shading shows one standard deviation on each side of the mean value. The GDI distribution is quite homogeneous (shown at -21° ATDC in Fig. B1 of Appendix B). The GDI distribution changes little between -21° ATDC and -5° ATDC; therefore, the GDI distribution is not presented here. Because the low-temperature reactions occur prior to the image acquisition time, it is likely that, under combusting conditions, much of the n-heptane will be consumed by -5° ATDC. Thus, the fuel distributions at this time correspond to a representative mixture distribution that tracks the fuel species present earlier in the cycle.

The case with an SOI timing of -145° shows a relatively small distribution in PRF number, with a range of PRF numbers from 59 to 65. However, the equivalence ratio map shows that a gradient in equivalence ratio is still present. The maximum equivalence ratio, $\phi = 0.55$, is located near the cylinder liner. Figure 11 shows that this gradient is primarily in the axial direction. The gradient in equivalence ratio is the result of the axial gradients in the equivalence ratio from the common-rail fuel distribution, and to a smaller extent, the equivalence-ratio gradient of the GDI distribution. It is possible that the apparent gradient in equivalence ratio (and PRF number) is partially the result of attenuation of the laser sheet. However, the calibration images showed only weak attenuation along the laser sheet. Additionally, the calibration procedure accounts for laser sheet attenuation to the degree that it occurs in the calibration image.

Retarding the n-heptane injection timing to -50° ATDC increases the stratification of both equivalence ratio and reactivity (PRF number). The PRF range spans from 60 in the downstream region of the jet, near the cylinder liner, to around 85 near the front edge of the field-of-view (~30 mm from the common-rail injector). The equivalence ratio ranges from a maximum of $\phi = 0.55$ near the liner to a minimum of $\phi = 0.25$ in the upstream region. Notice that retarding the injection timing from -145° to -50° ATDC causes the near-liner region to become richer and more reactive (i.e., lower PRF number) while the region closer to the common-rail injector becomes leaner and less reactive (i.e., higher PRF number). Hence, with the later common-rail injection, the mixing times are reduced such that the n-heptane is less uniformly mixed throughout the chamber and gradients in both PRF number and equivalence ratio are greater. The increase in equivalence ratio and PRF stratification is consistent with the reduction in the peak AHRR of the SOI -50° ATDC case. Further, the gradient in fuel reactivity (PRF) for the SOI -50° ATDC case correlates with the direction of reaction zone growth. Recall that the reaction zone tends to begin in the outer region of the chamber and move inward. Thus, it appears that the span of the gradient in fuel reactivity (and equivalence ratio) controls the peak heat-release rate and the direction of the gradient in fuel reactivity controls the direction of reaction zone growth.

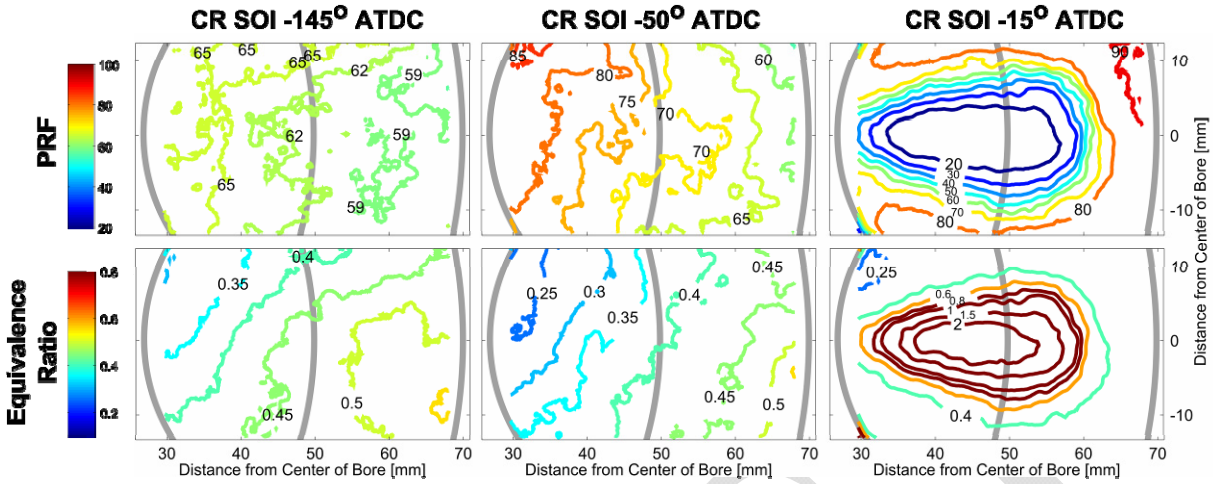

Figure 10. Ensemble-averaged PRF and equivalence ratio distributions acquired at -5° ATDC for cases with injection timings of -145°, -50°, and -15° ATDC.

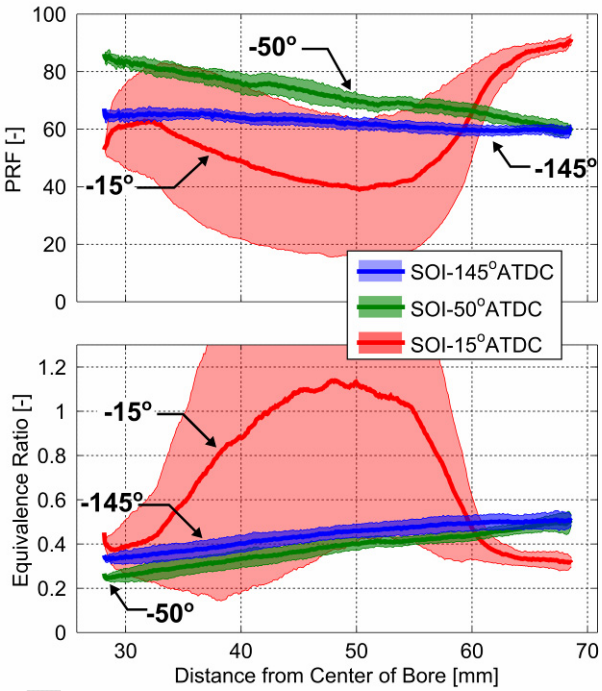

Figure 11. Average PRF and equivalence ratio at -5° ATDC as a function of axial distance from the common-rail injector. The solid lines show the average equivalence ratio at each axial distance from the common-rail injector and the shading shows ± one standard deviation (i.e., showing a measure of the spread in the radial direction).

The primary difference between the cases with SOI timings of -145° and -50° ATDC is the level of fuel reactivity stratification in the axial direction. In contrast, the case with an SOI timing of -15° ATDC shows a much different fuel distribution. The earlier SOI cases had sufficient time to "mix-out" the gradients in the radial direction. However, the case with an SOI timing of -15° ATDC shows strong gradients both in the axial and radial directions and a fuel distribution typical of a diesel jet – notice the large deviation from the axial average for the SOI -15° case shown in Figure 11. The peak equivalence ratio of the ensemble-averaged images at -5°

ATDC is greater than $\phi = 2.6$[2]. The high equivalence ratio region in the center of the jet corresponds to the region where high intensity luminosity was observed in the combusting cases, providing evidence that the bright regions in the luminosity images are the result of natural soot incandescence. Regions near the stoichiometric band around the outer edge of the n-heptane jet are likely to result in high NOx emissions. Similar to the equivalence ratio distribution, the PRF distribution of the SOI -15° ATDC case is broad with a maximum PRF number approaching 100 (i.e., neat iso-octane outside of the n-heptane jet) and a minimum PRF number of ~10 near the jet center. Although the PRF gradient of the SOI -15° ATDC is much larger than that of the SOI -50° ATDC case, the SOI -15° ATDC case shows more rapid heat release and a peak heat-release rate similar to that of the earliest injection timing case. Thus, increasing the gradient in PRF number does not always decrease the peak heat-release rate. In fact, the present study shows that over stratification significantly increases the peak heat-release rate.

The change in combustion characteristics with changing stratification may be explained according to the influence of equivalence ratio and PRF number on ignition delay. Figure 12 shows constant-volume ignition-delay calculations performed using the SENKIN code [29] with a closed reactor and a reduced PRF mechanism [30] at conditions representative of TDC for the current experiments for a range of PRF blends and equivalence ratios. Two regions are identified in Figure 12 according to the behavior of ignition delay. Regions with equivalence ratios less than about 0.6 show a relatively strong dependence of ignition delay on both equivalence ratio and the PRF blend of the fuel, while richer regions show much weaker dependencies.

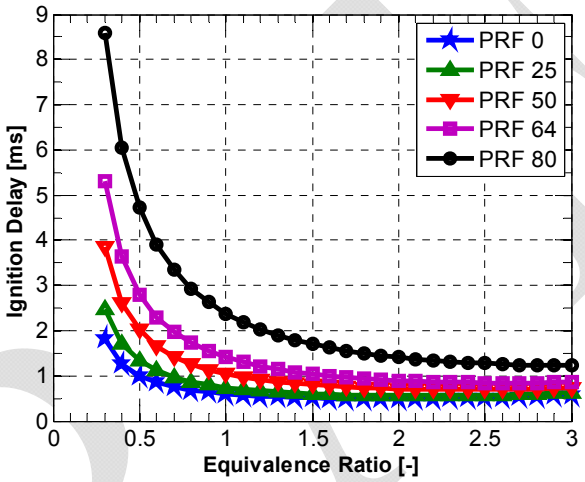

Figure 12. Constant-volume ignition delay calculations illustrating the effect of equivalence ratio and PRF number on ignition delay. The initial conditions correspond to representative TDC conditions from the current experiments (initial pressure = 27 bar, initial temperature = 837 K, and 21% intake oxygen concentration).

Revisiting the PRF and equivalence ratio maps of the SOI -15° ATDC case, it appears that the increase in heat-release rate is due to over stratification of the charge and is related to the quantity of fuel at equivalence ratios above ~0.6[3] (i.e., where the ignition delay is nearly constant). To quantitatively evaluate the fuel distribution, it is useful to analyze the single-shot images using mass weighted PRF and equivalence ratio histograms. The histogram were calculated from each single-shot image (40 images per set) and averaged to give a representative histograms for each injection timing. Figure 13 shows a mass-weighted histograms of the PRF number and equivalence ratio at -5° ATDC. Although these histograms are not representative of the entire combustion chamber, they do provide information about the fuel and fuel reactivity distributions in the downstream region of the jet (where ignition is generally observed).

[2] Note that the maximum equivalence ratio was capped at ten times the equivalence ratio of the calibration images. Therefore, the peak equivalence ratio in the images is shown to be 2.6; however, small regions have slightly higher equivalence ratios.

[3] At these operating conditions the ignition delay begins to increase around $\phi = 5$; however, the quantity of fuel at such high equivalence ratios in the present study is likely negligible.

The SOI -145° ATDC case has the narrowest PRF and equivalence-ratio histogram, which is consistent with the observed combustion characteristics and the ensemble-averaged images. Retarding the injection timing from -145° to -50° ATDC increases the widths of both the PRF and equivalence-ratio histograms, which helps to explain the reduced rate of heat release. As previously discussed, both PRF stratification and equivalence ratio stratification can be used to control the heat-release rate. At the present operating conditions, closed reactor simulations (see Appendix A for a detailed discussion) show that the PRF stratification has a larger influence on the ignition delay than the equivalence ratio stratification. The closed reactor simulations suggest that the reduction in the heat-release rate as the CR SOI is retarded from -145° ATDC to -50° ATDC is primarily due to increased PRF stratification.

The case with an SOI timing of -15° ATDC shows that the PRF histogram now spans nearly the entire PRF range and has a bimodal distribution with the most mass located at either very low PRF (high ϕ) or high PRF numbers (low ϕ). The equivalence ratio histogram shows that 31% of the imaged charge is located in an equivalence ratio band spanning from 0.6 to 2.6. This mass corresponds to a PRF range from 10 to 44, indicated by the shaded region of Figure 13. Revisiting the ignition delay plots for this equivalence ratio and PRF combination, it can be seen that the ignition delay only changes by ~0.5 ms (3.1 CA° at 1200 rpm) over this range. The PRF and equivalence ratio histograms confirm that the rapid energy release of the case with an SOI timing of -15° ATDC is the result of an over-stratified charge where 31% of the fuel mass is located in an equivalence ratio – PRF band where the ignition delay is nearly constant. Further, recall that the heat release curve for the SOI -15° ATDC case showed a tail extending late into the cycle. The tail on the heat release curve may be a sign of regions struggling to reach complete combustion. It is likely that these regions are located in the low-equivalence ratio (high PRF number) range of Figure 13. Indeed, metal-engine experiments **[28]** performed at a similar condition showed very high hydrocarbon emissions for the late injection timing case. The rapid heat release and weak late cycle burnout of the SOI -15° ATDC case show that operation in the RCCI mode with near TDC injection timings will likely result in poor engine performance due high combustion rates and low combustion efficiency.

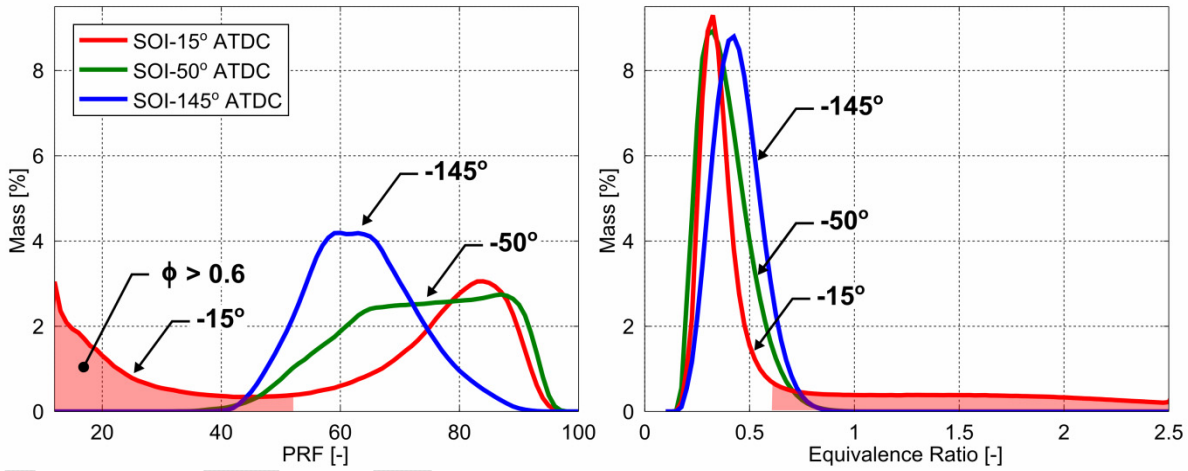

Figure 13. Mass weighted histograms of the PRF number and equivalence ratio calculated from the single-shot images

Notice that, compared to the ensemble-averaged fuel distributions, the histograms show a wider spread of both PRF number and equivalence ratio. This is expected since the ensemble averaging tends to smooth local inhomogeneities in the fuel distribution. Although the ensemble averaging tends to smooth the images, it is easier to interpret the average images than the single shot images. However, local ignition characteristics are likely controlled by the local inhomogeneities in the fuel distribution. Thus, Figure 14 shows a comparison of the ensemble-averaged and single-shot PRF images. Because the GDI fuel distribution and the common-rail fuel distribution were not acquired simultaneously, the images correspond to single-shot images from the common-rail injector assuming that the average distribution from the GDI injector remains constant. It is expected that the primary source of inhomogeneity comes from the common-rail injector; thus, this method was deemed acceptable. The single-shot images were selected by comparing the mass weighted equivalence ratio and PRF histograms of each single shot image to the histograms of the average image for each case. The top row shows the image with the most similar histogram and the bottom row shows the image with the least similar histogram. In general, the average images have similar features to the single-shot images; however, the smoothing of local inhomogeneities is clearly present in the averaged images. Focusing on the SOI -50° ATDC case, the single-shot PRF images show small isolated pockets of low PRF mixtures surrounded by regions of significantly higher PRF number. Recall that the chemiluminescence imaging showed small isolated ignition pockets that tended to appear and merge as the reaction zone moved upstream. It appears that the auto-ignition pockets observed in the chemiluminescence imaging are controlled by the isolated pockets

of highly reactive fuel (shown in the single-shot images) and the overall direction and rate of the reaction zone growth is controlled by the overall gradient in fuel reactivity (most clearly apparent in the ensemble-averaged images).

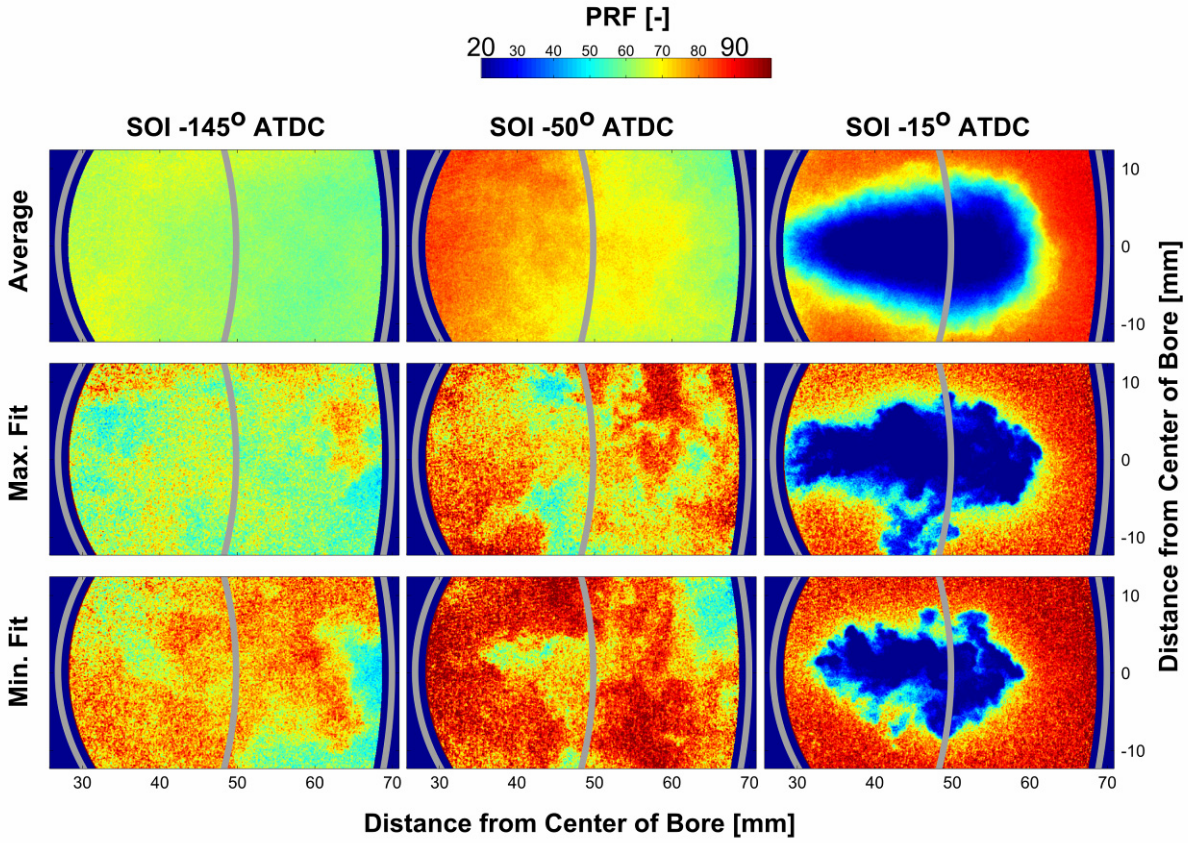

Figure 14. Comparison of ensemble-averaged and single shot PRF images. The top row shows the average image, the middle row shows the single-shot image with a histogram that is most similar to the histogram of the average image, and the bottom row shows the PRF map with a histogram most dissimilar to the histogram of the average image.

CONCLUSIONS

High-speed chemiluminescence imaging and toluene fuel-tracer PLIF were used explore fuel reactivity stratification as a method to control the rate of heat release for PCI combustion. A sweep of the common-rail injection timing was used to vary the level of fuel reactivity stratification. The injection timing sweep showed that the peak heat-release rate is highest for either early or late common-rail injections of n-heptane, and a minimum was found at mid-range injection timings near -50° ATDC. At very early injection timings, the chemiluminescence imaging showed HCCI-like combustion with random ignition locations and rapid combustion zone growth. The fuel-tracer imaging showed that the fuel distribution for the early injection timing case has only a weak spatial gradient in fuel reactivity.

Retarding the injection timing to -50° ATDC resulted in a significant reduction in the peak heat-release rate. At this mid-range injection timing, the chemiluminescence imaging showed ignition occurring in the downstream portion of the jet and a controlled reaction zone growth upstream toward the common-rail injector (i.e., toward the center of the combustion chamber). Consistent with the observed ignition location and reaction-zone growth, the fuel-tracer fluorescence imaging showed that the region with the highest fuel reactivity was located near the liner and the reactivity decreased closer to the center of the combustion chamber. The reduction in the peak AHRR appears to be the result of increased fuel reactivity stratification.

Similar to the early injection timing case, the case with a near-TDC injection of n-heptane (SOI = -15° ATDC) showed violent combustion in the early part of the heat release. Near the end of the heat release, the late injection timing case showed a tail. The tail on the heat release suggests that, in some regions of the chamber, reactions are occurring slowly. The combustion luminosity imaging

showed that ignition occurs in the downstream portion of the n-heptane jet and very quickly luminosity was observed throughout the entire n-heptane jet (i.e., the entire jet ignites nearly instantaneously). The fuel-tracer fluorescence imaging showed a bi-modal distribution in both equivalence ratio and PRF number. Ignition delay calculations suggest that the rapid energy release inside the jet is due to the limited mixing time that yields an over-stratified charge where much of the fuel mass is located in a region of nearly constant ignition delay. Further, the tail on the heat-release curve appears to be related to regions outside of the n-heptane jet where the mixture is primarily iso-octane near an equivalence ratio of 0.27. These regions have low fuel reactivity and may be the cause of high hydrocarbon emissions observed in complimentary metal engine experiments.

The single-shot images showed isolated pockets of high-reactivity fuel (i.e., low PRF number), which likely correspond to the isolated ignition pockets observed in the chemiluminescence imaging. The ensemble-averaged images show a strong correlation between the level of fuel reactivity stratification and the overall direction and rate of the reaction zone growth. This finding confirms that the rate of energy release can be controlled by controlling the stratification in the fuel reactivity using in-cylinder fuel blending. However, care must be taken to avoid over- and under-stratified operation, both of which can result in rapid energy release and excessive pressure rise rate.

ACKNOWLEDGEMENTS

The optical engine experiments were performed at the Combustion Research Facility, Sandia National Laboratories, Livermore, CA. Support for this research was provided by the U.S. Department of Energy, Office of Vehicle Technologies. Sandia is a multi-program laboratory operated by Sandia Corporation, a Lockheed Martin Company for the United States Department of Energy's National Nuclear Security Administration under contract DE-AC04-94AL85000. Financial support from the US Department of Energy (DOE) HCCI contract # DE-FC04-02AL67612 and from the Engine Research Center's Diesel Engine Research Consortium (DERC) member companies is gratefully acknowledged. The authors also express their gratitude to David Cicone of Sandia National Laboratories for his assistance with maintaining the optical-access research engine used in these experiments.

REFERENCES

1. Manente, V., Tunestal,P., and Johansson,B, **"**Partially Premixed Combustion at High Load using Gasoline and Ethanol, a Comparison with Diesel," SAE 2009-01-0944, 2009.
2. Splitter, D.A., Hanson,R.M., Kokjohn,S.L., and Reitz,R.D, "Reactivity Controlled Compression Ignition (RCCI) Heavy-Duty Engine Operation at Mid-and High-Loads with Conventional and Alternative Fuels," SAE 2011-01-0363, 2011.
3. Kokjohn, S.L., Hanson, R.M., Splitter, D.A., and Reitz, R.D., "Experiments and Modeling of Dual-Fuel HCCI and PCCI Combustion Using In-Cylinder Fuel Blending," *SAE Int. J. Engines* 2(2):24-39, 2010.
4. Manente, V., Tunestal, P., Johansson, B., and Cannella, W., "Effects of Ethanol and Different Type of Gasoline Fuels on Partially Premixed Combustion from Low to High Load," SAE Technical Paper 2010-01-0871, 2010.
5. Hasegawa, R. and Yanagihara, H, "HCCI Combustion in a DI Diesel Engine," SAE *2003-01-0745*, 2003.
6. Hardy, W.L. and Reitz,R.D, "A Study of the Effects of High EGR, High Equivalence Ratio, and Mixing Time on Emissions Levels in a Heavy-Duty Diesel Engine for PCCI Combustion," SAE 2006-01-0026, 2006.
7. Opat, R., Ra, Y., Gonzalez, M.A., Krieger, R., Reitz, R.D., Foster, D.E., Siewert, R., and Durrett, R., "Investigation of Mixing and Temperature Effects on HC/CO Emissions for Highly Dilute Low Temperature Combustion in a Light Duty Diesel Engine," SAE 2007-01-0193, 2007.
8. Bessonette, P.W., Schleyer, C.H., Duffy, K.P., Hardy, W.L., and Liechty, M.P., "Effects of Fuel Property Changes on Heavy-Duty HCCI Combustion," SAE 2007-01-0191, 2007.
9. Inagaki, K., Fuyuto,T., Nishikawa,K., Nakakita,K., and Sakata,I., "Dual-Fuel PCI Combustion Controlled by in-Cylinder Stratification of Ignitability," SAE 2006-01-0028, 2006.
10. Kokjohn, S. L. and Reitz, R. D., "A Modeling Study of Charge Preparation in an HCCI Engine using a Variable Pressure Pulse (VPP) Injection System and Optimized PRF Blends," 11th International Conference on Liquid Atomization and Spray Systems, Vail, Colorado USA, July 30, 2009.

11. Hanson, R. M., Kokjohn, S. L., Splitter, D. A., and Reitz, R. D., "An Experimental Investigation of Fuel Reactivity Controlled PCCI Combustion in a Heavy-Duty Engine," *SAE Int. J. Engines* 3(1):700-716, 2010.
12. Hanson, R. M., Kokjohn,S. L., Splitter,D. A., and Reitz,R. D., "Low Load Investigation of Reactivity Controlled Compression Ignition (RCCI) Combustion in a Heavy-Duty Engine," SAE 2011-01-0361, 2011.
13. Kokjohn, S. L., Hanson,R. M., Splitter,D. A., Kaddatz, J., and Reitz,R. D. "Fuel Reactivity Controlled Compression Ignition (RCCI) Combustion in Light- and Heavy-Duty Engines," *SAE Int. J. Engines* 4(1):360-374, 2011.
14. Splitter, D. A., Hanson, R. M., Kokjohn, S. L., Rein, K., Sanders, S., and Reitz, R. D., "An Optical Investigation of Ignition Processes in Fuel Reactivity Controlled PCCI Combustion," *SAE Int. J. of Engines*, 3(1):142-162, 2010.
15. Kokjohn, S.L., Hanson, R.M., Splitter, D.A., and Reitz, R.D., "Fuel Reactivity Controlled Compression Ignition (RCCI): A Pathway to Controlled High-Efficiency Clean Combustion," *International Journal of Engine Research*, Special Issue on Fuel Efficiency, 12:209-226, 2011.
16. Kokjohn, S.L. and Musculus, M.P.B. Reitz, R.D., "Chemiluminescence and Fuel PLIF Imaging of Reactivity Controlled Compression Ignition (RCCI) Combustion," ILASS Americas, 23rd Annual Conference on Liquid Atomization and Spray Systems, Ventura, CA, May 15-18. 2011.
17. Dec, J. E., "A Conceptual Model of DI Diesel Combustion Based on Laser-Sheet Imaging," *SAE Transactions,* 106(3):1319-1348, 1997.
18. Musculus, M.P.B, "On the Correlation between NOx Emissions and the Diesel Premixed Burn," SAE 2004-01-1401, 2004.
19. Genzale, C., Reitz, R. D., and Musculus, M.P.B., "Effects of Piston Bowl Geometry on Mixture Development and Late-Injection Low-Temperature Combustion in a Heavy-Duty Diesel Engine," *SAE Int. J. Engines* , 1(1):913-937, 2008.
20. Heywood, J. B, Internal Combustion Engine Fundamentals. McGraw-Hill, 1988.
21. Hultqvist, A., Christensen, M., Johansson, B., Franke, A., Richter, M., and Aldén, M., "A Study of the Homogeneous Charge Compression Ignition Combustion Process by Chemiluminescence Imaging," SAE 1999-01-3680, 1999.
22. Hwang, W., Dec, J.E., and Sjöberg, M., "Fuel Stratification for Low-Load HCCI Combustion: Performance and Fuel-PLIF Measurements," *SAE Transactions*, 116(3):1437-1460, 2007.
23. Musculus, M.P.B., Lachaux, T., Pickett, L. M., and Idicheria, C. A., "End-of-Injection Over-Mixing and Unburned Hydrocarbon Emissions in Low-Temperature-Combustion Diesel Engines," *SAE Transactions*, 116(3):515-541, 2007.
24. Schulz, C. and Sick,V, "Tracer-LIF Diagnostics: Quantitative Measurement of Fuel Concentration, Temperature and Fuel/Air Ratio in Practical Combustion Systems," *Progress in Energy and Combustion Science*, 31(1):75-121, 2005.
25. Sjöberg, M. and Dec, J.E., "An Investigation of the Relationship between Measured Intake Temperature, BDC Temperature, and Combustion Phasing for Premixed and DI HCCI Engines," *SAE Transactions*, 113(3):1271-1286, 2004.
26. Dec, J.E. and Hwang, W., "Characterizing the Development of Thermal Stratification in an HCCI Engine using Planar-Imaging Thermometry," *SAE Int. J. of Engines*, 2(1):421-438, 2009.
27. Sjoberg, M. and Dec,J., "Smoothing HCCI Heat-Release Rates using Partial Fuel Stratification with Two-Stage Ignition Fuels," SAE 2006-01-0629, 2006.

28. Splitter, D.A., Hanson, R.M., Kokjohn, S.L., Wissink, M, and Reitz, R.D., "Injection Effects in Low Load RCCI Dual-Fuel Combustion A Scaling Study of Reactivity Controlled Compression Ignition (RCCI) Operation in Light and Heavy-Duty Engines," SAE 2011-24-0047, 2011.
29. Lutz, A. E., Kee,R. J., and Miller,J. A., "SENKIN: A FORTRAN Program for Predicting Homogeneous Gas Phase Chemical Kinetics with Sensitivity Analysis," SAND87-8248, 1996.
30. Ra, Y. and Reitz, R.D., "A Reduced Chemical Kinetic Model for IC Engine Combustion Simulations with Primary Reference Fuels," *Combustion and Flame*, 155(4):713-738, 2008.

CONTACT INFORMATION

Sage Kokjohn
Department of Mechanical Engineering
University of Wisconsin-Madison
Madison, WI 53706 USA
Phone: 608.265.8608
Email: kokjohn@wisc.edu

DEFINITIONS/ABBREVIATIONS

ATDC	After Top Dead Center
AHRR	Apparent Heat-release rate
BTDC	Before Top Dead Center
BDC	Bottom Dead Center
CCD	Charge Coupled Device
CR	Common-rail
CMOS	complementary metal oxide semiconductor
CFD	Computational Fluid Dynamics
CA50	Crank Angle at 50% Burn
DI	Direct Injection
EGR	Exhaust Gas Recirculation
FOV	Field-of-view
FTIR	Fourier-Transform Infrared
GDI	Gasoline Direct Injection
HSC	High Speed Camera
HTHR	High Temperature Heat Release
HPLC	high-performance liquid chromatography
HCCI	Homogeneous Charge Compression Ignition
IMEP	Indicated Mean Effective Pressure
LIF	Laser Induced Fluorescence
LED	Light Emitting Diode
LWP	Long Wave Pass

LTHR	Low Temperature Heat Release
PLIF	Planar Laser Induced Fluorescence
PCI	Premixed Compression Ignition
PRR	Pressure Rise Rate
PRF	Primary Reference Fuel
RCCI	Reactivity Controlled Compression Ignition
SWP	Short Wave Pass
SOI	Start of Injection
TDC	Top Dead Center
UV	Ultra Violet

APPENDIX A

RELATIVE ROLES OF EQUIVALENCE RATIO AND FUEL REACTIVITY STRATIFICATION

The discussion in the body of the paper showed that it is possible to control the combustion rate using in-cylinder fuel blending to introduce stratification in both the equivalence ratio and PRF distributions when the SOI timing was more advanced than -50° ATDC. Because both equivalence ratio stratification and PRF stratification are present, it is of interest to understand the relative roles of equivalence ratio and PRF stratification for controlling highly-premixed combustion. To simplify the discussion, the PRF number is defined here as the mass fraction of iso-octane in the charge (i.e., neglecting the small density differences of n-heptane and iso-octane), the premixed fuel is assumed to be homogenously distributed iso-octane, and the direct-injected fuel is assumed to be n-heptane. With these simplifying assumptions, the PRF number can be related to the local equivalence ratio, ϕ_{local}, and premixed equivalence ratio, ϕ_{premix}, as

$$\phi_{local} = 100\frac{\phi_{premix}}{PRF} \quad \textbf{(A1)}$$

Using Eq. A1, the relative roles of equivalence ratio and fuel reactivity stratification are evaluated using constant-volume ignition-delay calculations performed with SENKIN **[29]** and a reduced PRF mechanism **[30]**. The results with an initial temperature of 837 K, a pressure of 27 bar, and a premixed equivalence ratio of 0.27 are shown in Figure A1. Equivalence ratios from 0.27 (i.e., the premixed fuel) to 0.5 were evaluated. While Figure A1 is helpful to isolate the effects ϕ and PRF stratification, the results should be interpreted with caution since they represent the ignition delay of an isolated mixture (i.e., with no interaction from the surrounding regions). Even without considering the effects of transport, the ignition delay of the less reactive regions (i.e., higher PRF number or lower equivalence ratio) will decrease due to compression heating. In the limit of isolated mixtures, Figure A1 shows that increasing the equivalence ratio from 0.27 to 0.48 at a constant PRF 64 results in a decrease in ignition delay of ~20 crank angle degrees at 1200 rev/min. However, over the same equivalence ratio range, the PRF number ranges from 100 (i.e., the premixed iso-octane) to around 55. The effect of equivalence ratio and PRF stratification are complimentary and in the case of PRF stratification, the change in ignition delay is over 100 crank angle degrees at 1200 rev/min. As previously discussed, the presented change in ignition delay represents the maximum change in ignition delay considering isolated conditions. However, Figure A1 clearly demonstrates that, in terms of controlling fuel reactivity, the PRF stratification dominates the equivalence ratio stratification.

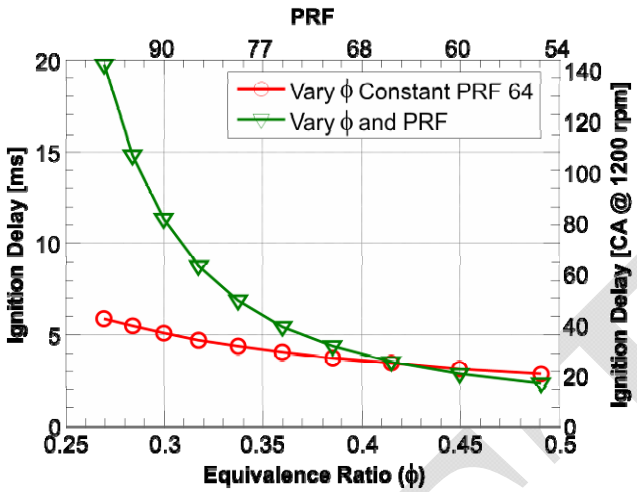

Figure A1. Constant volume ignition delay calculations used to evaluate the relative roles of equivalence ratio and PRF stratification. The premixed fuel has an equivalence ratio of 0.27.

APPENDIX B

PRF AND EQUIVALENCE RATIO MAPS PRIOR TO LTHR

Figure B1 shows contours of the equivalence ratio distribution created by the GDI injector measured using fuel-tracer fluorescence imaging and the average equivalence ratio as a function of distance from the center of the bore (i.e., axially along the path of the common-rail injector jet). The GDI equivalence ratio distribution confirms that, although small inhomogeneities are present, the fuel delivered through the GDI is reasonably well mixed by prior to ignition. The GDI equivalence ratio ranges from a maximum of 0.3 near the liner to around 0.24 closer to the cylinder centerline. Recall that if the iso-octane delivered in the GDI pulse were homogeneously mixed, the equivalence ratio would be 0.27. The average equivalence ratio in the field-of-view from the fuel tracer fluorescence image of the GDI injection is indeed 0.27, which provides some confidence in the fuel distribution measurements.

Figure B2 shows ensemble-averaged PRF and equivalence ratio distributions at -21° ATDC and Figure B3 shows the corresponding average PRF and equivalence ratio as a function of axial distance from the injector for the three selected cases . Note that the case with a common-rail injection timing of -15° ATDC is included for completeness; however, for this case, the common-rail injection event has not yet started and the fuel distribution is equivalent to the GDI distribution presented in Figure B1. The case with an SOI timing of -145° shows a relatively small distribution in PRF number, with a range of PRF numbers from 58 to 67. However, the equivalence ratio map shows that a gradient in equivalence ratio is still present. The maximum equivalence ratio, $\phi = 0.55$, is located near the cylinder liner. Figure B2 shows that this gradient is primarily in the axial direction. Similar to the images acquired later in the cycle, the PRF and equivalence-ratio distributions for the case with an SOI timing of -50° ATDC show increased equivalence-ratio and PRF stratification. The PRF range spans from 55 in the downstream region of the jet, near the cylinder liner, to around 90 near the front edge of the field-of-view (~30 mm from the common-rail injector). The equivalence ratio ranges from a maximum of $\phi = 0.6$ near the liner to a minimum of $\phi = 0.25$ in the upstream region. As the injection timing is retarded from -145° ATDC to -50° ATDC, the upstream region of the jet becomes leaner and less reactive (i.e., higher PRF number) while the downstream region becomes richer and more reactive (i.e., lower PRF number).

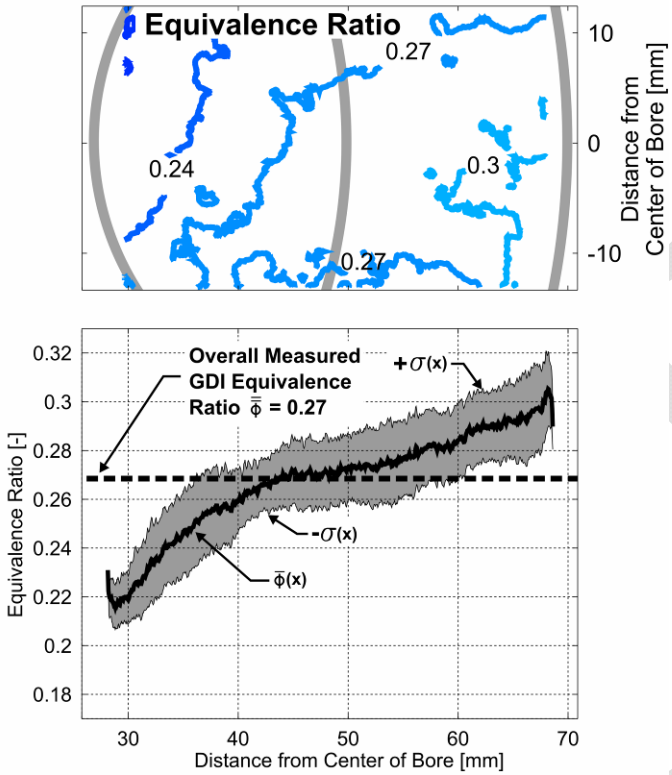

Figure B1. Equivalence ratio distribution created by the GDI injection as a function of distance from the bore center at -21° ATDC. Note that if the GDI injection were homogenously mixed, the equivalence ratio would be 0.27.

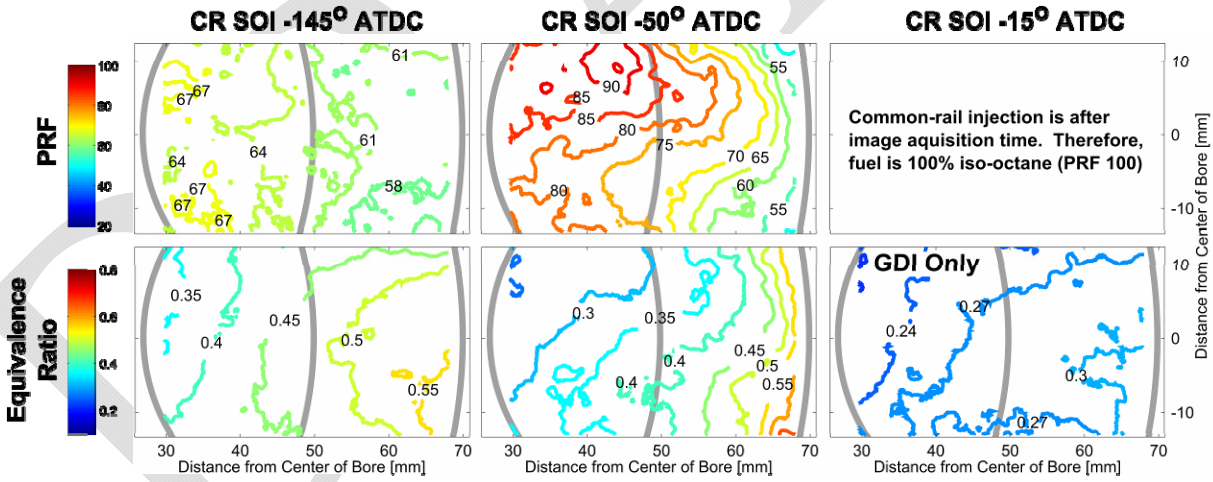

Figure B2. Ensemble-averaged PRF and equivalence ratio distributions acquired at -21° ATDC for cases with injection timings of -145°, -50°, and -15° ATDC. Note that the case with an SOI of -15° ATDC only shows the equivalence ratio distribution from the GDI injector.

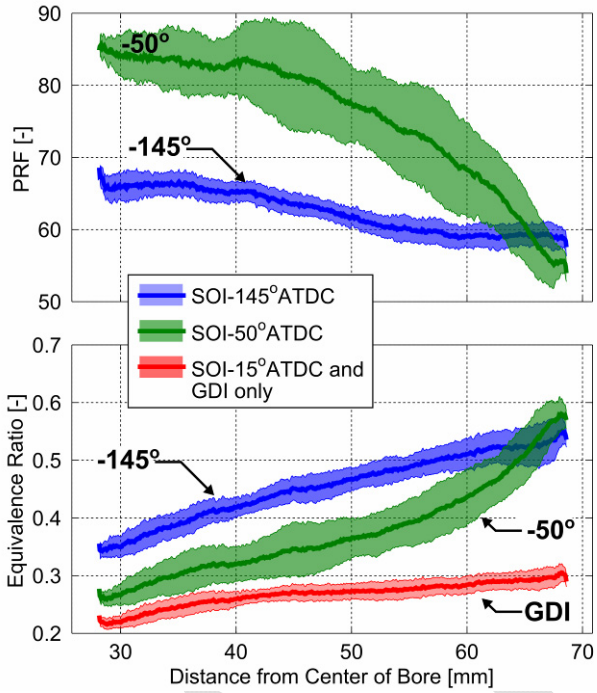

Figure B3. Average PRF and equivalence ratio at -21° ATDC as a function of axial distance from the common-rail injection. The solid lines show the average equivalence ratio at each axial distance from the common-rail injector and the shading shows ± one standard deviation (i.e., showing a measure of the spread in the radial direction). Note that the GDI PRF is 100 (neat iso-octane) and is not shown in the PRF plot.